# Supporting Information

## Salami et al. 10.1073/pnas.1410233111

### SI Text

**Normalization of Functional MRI Data Using DARTEL.** The supervised voxel-based morphometry protocol proceeded in the following stages to normalize both fMRI and structural data. Motion-corrected fMRI data were first rigidly aligned to T1-weighted images. T1-weighted images were segmented into gray matter (GM) and white matter (WM) using a new segmentation algorithm in SPM8. Then, a group-specific template (across all subjects) was created using diffeomorphic anatomical registration using exponentiated lie algebra [DARTEL (1)]. This was done by first importing tissue class images (e.g., GM, WM) into the DARTEL space using the normalization parameter yielded during the segmentation step followed by resampling to isotropic voxels ($1.5 \times 1.5 \times 1.5$ mm). Then, the imported images went through an iterative procedure that began by producing an initial template as a mean of GM/WM across all participants ($n = 339$). Deformation from the initial template to each of the subject-specific GM/WM images was computed and the inverse of the deformation was applied to each of the subject-specific GM/WM images. A second template was then created as the mean of the deformed subject-specific GM/WM images across all participants, and this procedure was repeated until a sixth template was created. Finally, the coregistered fMRI images and segmented GM/WM images were nonlinearly normalized, subject by subject, to the sample-specific template (using a subject-specific flow field), affine-aligned into a Montreal Neurological Institute template, and finally smoothed using an 8.0-mm full width at half maximum Gaussian filter. Thus, both preprocessed structural MRI and fMRI images were in the same space and had the same voxel size ($2 \times 2 \times 2$ mm).

**Independent Component Analysis.** ICA is a multivariate approach that identifies spatially independent and temporally coherent patterns of the brain from their linearly mixed fMRI signal. As such, ICA provides a natural measure of functional connectivity (i.e., each component consists of a set of brain regions that shares the same temporal pattern). In the current study, group ICA was performed using the GIFT toolbox (2). In the first step, a time series of each voxel was normalized by its average intensity. This intensity normalization procedure improves the accuracy and test–retest reliability of subsequent ICA output (2). The intensity-normalized preprocessed data for all participants ($n = 339$) were concatenated across time. After temporal concatenation, the optimal number of independent sources was estimated using a minimum description length (MDL) algorithm. As such, 47 independent components (ICs) were estimated. Two-step data reduction was carried out using principal component analysis (PCA). In the first step, subject-specific data reduction was conducted to reduce computational complexity while preserving most of the information content of the data (100 principal components were retained). The second (group-level) data reduction was again carried out by PCA according to the estimated number of ICs (i.e., 47 estimated by MDL). After data reduction, the Infomax ICA algorithm (3) was used to optimally extract 47 ICs. The latter procedure was repeated 20 times using the ICASSO toolbox (4), and the resulting components were clustered to estimate the reliability of the ICs. All ICs reported in the current study exhibited a reliability index ($I_q$; ranges from 0 to 1) greater than 0.95. Finally, a backreconstruction using the recently developed GICA3 method (an improved version of dual regression) was conducted (2), by which time courses (TCs) and spatial maps (SMs) were computed for each subject (both TCs and SMs have the same unit, percent signal changes; for more details, see *ICA-Driven Measures of RSNs*). There are desirable properties in GICA3 not available in the other method, including that the aggregate SM is the sum of the subject-specific SMs, analogous to a random effects model where the subject-specific effects are zero-mean distributed deviations from the group mean effect. As such, it was shown that noise-free ICA using GICA3 provides more robust results with a more intuitive interpretation (5). As for the model order, the estimation of dimension for fMRI data is still an open and challenging problem, although it has been shown that both analytic approaches using information theoretic criteria (such as MDL) and empirical methods provide reasonable results (6). Previous studies suggested that an appropriate model order can be empirically estimated from the $I_q$ curve such that the point at which components transition from relatively stable to less reliable can be considered as a reasonably good estimate of the model order (7, 8). Based on this suggestion, we varied the model order from 30 to 70 and again found 47 to be the knee (i.e., transition point) in the $I_q$ curve. Finally, we also varied the model order from 30 to 70, and found that the functional architecture of the default mode network remained relatively stable across different model orders. Taken together, although we cannot be certain that we have the true model order, both analytical and empirical approaches suggested that 47 components could be a reasonable estimate (Fig. S3).

**Resting-State Network Selection.** After visually inspecting the group average maps, ICs located in the cortex exhibiting low spatial overlap with the typical topology of potential artifacts (e.g., vascular, ventricle, motion, and susceptibility artifacts) and representing functionally meaningful patterns were considered to be RSNs (Fig. S1; refs. 2, 9–14). In addition, a template-matching procedure was carried out using templates of established RSNs provided online by the developers of the GIFT program (2). For the hippocampus IC reported in this study, however, no RSN has been identified in the noted template. Instead, spatial correlation was conducted with a corresponding network reported in other studies (9, 15). To further substantiate our categorization (RSNs vs. physiological artifacts), spectra were characterized with a metric of low- to high-frequency power ratios (PRs) used previously by Allen and colleagues (2). ICs that exhibited a higher PR (>7) were considered to be robust RSNs. It is important to stress that although we found 24 RSNs, the main focus of the current paper is on the cortical and the HC DMN components.

Finally, a voxelwise one-sample $t$ test was computed across all subjects (each subject as a random effect) for all RSNs, thereby providing a statistical threshold on RSNs. Thresholds were based on the distribution of voxelwise $t$ statistics to identify voxels reliably and consistently activated across subjects using a gamma-mixture model fit controlling for a false-discovery rate (FDR) of 1%.

**ICA-Driven Measures of RSNs.** For the set of selected RSNs (and in particular focus for the DMN), we considered four ICA-driven measures that reflect distinct but complementary facets of RSNs. (*i*) Component SMs reflected the level of coactivation (connectivity) within a network in a voxelwise manner (voxelwise connectivity). An SM was created after the backreconstruction step of the group ICA, which creates subject-specific maps from a corresponding group-level IC. (*ii*) Global indices of functional connectivity reflected connectivity within a network as a whole.

This measure was computed according to work by Glahn and colleagues (16). In short, individual 3D subject-specific SMs for each network were concatenated into a single 4D map, and the first principal eigenvector representing the subject's connectivity was calculated within a study-specific mask of the corresponding network. The mask was generated with a Gaussian/gamma-mixture model fit to the intensity histogram of group ICA for each network, controlling for an FDR of 1%. (*iii*) The subject-specific amplitude of a TC indicated the level of activation within a network. As suggested in a recent paper by Allen and colleagues (6), the amplitude was computed as a joint metric (which combines scaling information from TCs and SMs) using the TC SD, a well-characterized indicator of the spread or dispersion across the entire network, and the SM maximum value, which exhibited the amplitude of the top 20 voxels (intensity was averaged to reduce the influence of noise) most strongly associated with the corresponding TC. Note that TCs were detrended and despiked. In addition, motion parameters were regressed out from each component's TC (i.e., post-ICA motion correction). (*iv*) The internetwork functional connectivity (IFC) reflected connectivity between networks (17). The IFC was estimated as Pearson's correlation coefficients between pairs of TCs that were detrended, despiked, and filtered using a fifth-order Butterworth low-pass filter ($f < 0.15$).

**Age-Related Differences in RSN Measures.** To investigate age-related differences in SM connectivity measures, a voxelwise general linear model was set up for each RSN. Age, sex (coded as a binary variable), age-by-sex interaction, temporal signal-to-noise ratio (tSNR) as a predictor of data quality, as well as a nuisance predictor related to motion were included in the model. Although ICA helped in identification of motion-related sources, which were excluded from further analysis (e.g., ref. 18), it has been shown that residual motion-related variance may still partly remain in an RSN (19, 20). For each subject, rigid-body motion was estimated using SPM's realignment routine. This estimation derives a motion transformation matrix for each time point that is described by six motion parameters consisting of three translations and three rotations. These six parameters were condensed to a scalar quantity, namely framewise displacement [FD (19)], which reflects instantaneous head motion from a frame to an adjacent frame. As a separate analysis, we computed three other possible metrics of head motion, namely maximum motion (maximum absolute translation of each brain volume compared with the previous volume), number of movements and rotation (number of relative displacements >0.1 mm in 3D space between adjacent volumes), and mean scan-to-scan translation and mean scan-to-scan rotation as suggested by Allen and colleagues (2). Consistent with a previous study (20), the use of different metrics did not change the results, and hence FD was used as the central metric of head motion in all analyses. In addition, tSNR of each resting-state session was computed, as suggested by Van Dijk and colleagues (20). The mean signal across the BOLD run was calculated for each voxel, and the mean value was divided by the SD of the signal intensity within the voxel over time. Finally, the mean tSNR across all voxels in the brain served as the measure of tSNR for the BOLD fMRI data. In all analyses, local maxima with $p < 0.05$ (FWE-corrected) with an extended threshold of 20 contiguous voxels ($K > 20$) were considered to be significant. To investigate age-related differences in global measures of connectivity and amplitude, partial correlation was carried out between each measure and age (controlling for sex, motion parameter, and tSNR). Finally, those components that reflected reliable age differences across three main RSN outcome measures (global measures: $r \geq 0.20$, $p < 0.0001$; voxelwise measures: $p < 0.05$ [familywise error (FWE)-corrected], $k > 20$) were reported in the current study. As stated in the main text, the main focus of this paper was to thoroughly investigate the interplay among age, the DMN (both the cortical and HC subsystems), and episodic memory function. As such, it is reasonable to identify the DMN using a template-matching approach and use multiple-comparison correction methods that correct the results at the DMN component level. In a second, but more explanatory, attempt, we also investigated the effect of age on all 24 RSNs. (It is important to stress that these results are only supplementary and the main message of the paper, reported in the main text, should be considered independent from the additional analyses as presented here.)

Although we used a strict threshold to select the most age-sensitive RSNs (6 out of 24 components) at the global connectivity level (i.e., $p < 0.001$; corrected for multiple comparison), a second-level inter-RSN correction can further adjust for the risk of type 1 error (false positives) induced by increasing the number of components tested simultaneously. As such, we ran a control analysis as suggested in a paper by Abou Elseoud and colleagues (21) to further substantiate our supplementary findings. In short, temporally concatenated subject-specific maps of each RSN (24 RSNs in total) were spatially concatenated in the *y* direction. Then, 5,000 permutations were conducted on the concatenated map. Our results confirmed that voxels within the anterior and the posterior DMN reflected age-related connectivity decreases with aging (posterior DMN: xyz = −6 −26 24; anterior DMN: xyz = −6 40 54). Critically, we also observed age-related increased connectivity in the bilateral HC of the DMN (left HC: xyz = −18 −14 −18; right HC: xyz = 16 −10 −14). Finally, age-related decline in voxelwise connectivity was also observed for the bilateral fronto-parietal network (left: xyz = −30 24 48, −42 −56 50; right: xyz = 26 28 50, 42 −44 56) and the medial parietal network (xyz = −8 −52 68, 16 −74 54).

To better localize the HC component and its age-sensitive segment, the hippocampus proper of our DARTEL template was segmented by Freesurfer. A contour of the hippocampus proper was created and used in all analyses to better localize effects within the hippocampus proper. In addition to the voxels with elevated functional connectivity within the hippocampus proper (reported in the main text), voxels with decreased functional connectivity were also observed within the hippocampus proper (left HC: xyz = −34 −20 −18, $t = 5.60$; right HC: xyz = 30 −14 −20, $t = 5.58$). Critically, however, none of these voxels exhibited significant correlations with episodic memory performance, nor with longitudinal memory performance over 20 y even at a lenient threshold ($p < 0.01$, uncorrected), and thus were not considered for further analysis.

**Influence of Head Motion on Observed Age Effects on DMN Functional Connectivity.** Past studies have shown that head motion has significant, systematic effects on different measures of functional connectivity (19, 20). In particular, effects of head motion may be erroneously interpreted as age-related alterations of DMN's functional connectivity.

In the first set of analyses, global signal regression (GSR) and "scrubbing" (19) were conducted prior to ICA. To investigate whether a relatively small number of movements (e.g., bad frames) affected our main findings, an additional preprocessing step, scrubbing, was conducted. A detailed description of scrubbing is given in a study by Power and colleagues (19). In short, we identified the most egregiously suspect frames of our RS temporal data based on an FD measure. FD was computed from realignment parameters that were calculated during preprocessing of RS data, and frames with FD >0.3 (+2 SD for all displacements) were flagged and eliminated. We also tested other thresholds (e.g., +1 SD and +3 SD), which produced roughly the same results, although lower thresholds produced an excessive number of flagged frames (i.e., >35), which led to the exclusion of many subjects. All subjects (after scrubbing) contained at least 4 min of resting-state data, which were reported to be sufficient to

identify RSNs. ICA was then rerun on the preprocessed data. All identified RSNs (after scrubbing) showed strong spatial correlations ($r > 0.92$, $p < 0.0001$) with the RSNs reported in Fig. S1. Critically, the same RSNs were found to be age-sensitive. Thus, negative correlations with age were observed for the anterior and posterior DMN and positive correlations for the HC (Fig. S5 *A*–*C*).

In the second set of analyses, both individual-level GSR and motion correction using the Friston 24-parameter model were conducted (22) followed by ICA. Consistent with the results after scrubbing, 24 RSNs were identified (Fig. S2). For both the anterior and the posterior DMN, the results of the voxelwise connectivity index converged with the results of the amplitude and global connectivity indices in showing age-related decline (Fig. S5 *D* and *E*). For the HC network, the coupling between left and right HC was strengthened with advancing age, as shown by both the voxelwise and global connectivity (Fig. S5*F*). Similarly, there was an age-related increase in amplitude in the HC network.

Although we controlled for motion by using both scrubbing and the Friston model, several additional control analyses were performed to assure that our observation of age-related differences in functional connectivity of identified RSNs was independent of motion. First, we conducted a stepwise selection approach using MANCOVA (mialab.mrn.org/software/mancovan/index.html). For each RSN, the MANCOVA model predicting functional connectivity is F = DB + E, where F is the matrix of functional connectivity, D is the design matrix (including age, sex, and tSNR; FD is an estimate of motion), and E is the matrix of error. Backward selection was implemented such that the full model was compared (*F* test using the Wilks Lambda likelihood ratio test statistic) with each reduced model. The reduced model was defined by removing one column of the design matrix. The final reduced model has all terms significant at $\alpha = 0.01$. Results from a multivariate MANCOVA model selection strategy confirmed that for the seven age-sensitive RSNs only age and sex ($p < 0.05$), but neither motion nor tSNR, predicted functional connectivity. Second, we subdivided our sample into two age- and sex-matched groups with large (high-mover: $n = 169$; 62.36 ± 12.88 y of age, 92 females) and small (low-mover: $n = 169$; 60.56 ± 13.76 y of age, 92 females) motion according to a median-split analysis based on FD. There was no significant difference in age between the two groups ($p > 0.5$). We found no significant group difference in global connectivity and amplitude of DMN as well as HC RSN ($p > 0.2$). No significant group difference was found for the voxelwise connectivity. A similar finding was observed when a median-split analysis was carried out based on the mean scan-to-scan translation and mean scan-to-scan rotation as two alternative indices of head motion (2). Third, to compute the degree of motion relatedness of the brain mode time courses, six regressors modeling head motion [three translation ($T_x$ $T_y$ $T_z$) parameters and three rotation parameters ($R_{pitch}$ $R_{roll}$ $R_{yaw}$)] were created. These regressors were fit to the calibrated subject-specific TC of each RSN using a multiple-regression approach. Motion relatedness can be assessed by performing an analysis of the resulting fit parameters (23). That is, an RSN is considered motion-related if the regressor parameter fit survives a one-sample *t* test. Consistent with the previous control analyses, none of the age-sensitive networks (except a parietal–visual network) reflected significant associations with motion parameters. Specifically, none of the six head motion regressors were significantly associated with the TC of the posterior ($t_x = -0.43$; $t_y = 1.09$; $t_z = -0.37$; $t_{pitch} = -1.33$; $t_{roll} = -1.04$; $t_{yaw} = 0.28$; $p > 0.1$) and anterior ($t_x = -0.60$; $t_y = 0.78$; $t_z = 0.62$; $t_{pitch} = -1.19$; $t_{roll} = -1.34$; $t_{yaw} = 1.12$; $p > 0.1$) DMN. Similarly, no significant effect of motion was observed for the HC RSN ($t_x = -0.16$; $t_y = 1.13$; $t_z = -1.19$; $t_{pitch} = -0.33$; $t_{roll} = 0.94$; $t_{yaw} = 1.02$; $p > 0.1$). In addition, to control for both subject-specific motion correction using scrubbing and the Friston model and group-level motion (reported above), we applied a technique that derives estimates of displacement on a voxelwise basis (24). Using this approach, we computed a voxelwise map of motion for each subject that displayed how much a given voxel moved from the prior time point. To explore whether age-related differences in functional connectivity were driven by local changes due to motion, the biological parametric mapping (BPM) toolbox was used. Voxelwise motion maps served as a covariate in a general linear model (GLM). Of chief interest was to investigate whether the elevated hippocampal coupling in aging could be accounted for by age-related local changes in motion. Results showed that age-related increases (before including the voxelwise motion map: left HC: xyz = −18 −14 −18, $t_{334} = 9.33$; right HC: xyz = 16 −10 −14, $t_{334} = 5.63$) in voxelwise functional connectivity of the HC RSN persisted after controlling for voxelwise motion (after including the voxelwise motion map: left HC: xyz = −18 −14 −18, $t = 9.28$; right HC: xyz = 16 −10 −14, $t = 5.60$). In addition, no region within the HC network exhibited significant correlation between functional connectivity and motion ($r < 0.06$). Finally, to investigate the effect of age on non-RSN components, we ran a control analysis on a cerebral spinal fluid (CSF) component, which is a typical artifact that confounds RS data. The association between age and functional connectivity of the CSF component was weak [mean correlation: $r$ (CSF, age) = 0.09, $p > 0.05$]. This nonsignificant association substantiates the specificity of age effects on RSNs.

**Offline Behavioral Measures and RSNs.** All subjects underwent a neuropsychological assessment with the Betula test battery. The average time between the neuropsychological testing and scanning was 266 d. The offline measures included block design and several tests of episodic memory. Block design is a part of the Wechsler Adult Intelligence Scale and is generally considered to tax visuospatial processing (25). Episodic memory was assessed with a composite of five episodic memory scores, measured at 5-y intervals over a period of 20 y of the Betula study. The composite (summing across tests) consisted of (*i*) immediate free recall of 16 imperative verb–noun sentences that were enacted by the participant; (*ii*) delayed cued recall of nouns from the previously enacted sentences; (*iii*) immediate free recall of 16 verbally and visually presented verb–noun sentences; (*iv*) delayed cued recall of nouns from the previously presented sentences; and (*v*) immediate free recall of 12 verbally presented nouns.

To investigate the relation between RSN global measures of connectivity/amplitude and behavioral measures, Pearson's correlations were carried out between each RSN measure and offline behavioral measures separately (controlled by age, sex, FD movement parameter, and tSNR).

**Gray Matter Volume and RSNs.** To explore whether age-related differences in functional connectivity were driven by local GM atrophy, BPM (26) (fmri.wfubmc.edu/software/bpm) was used. Preprocessed voxelwise GM maps (see preprocessing and data analysis) served as a covariate in a GLM framework to investigate whether age-related changes in GM volume accounted for age-related differences in functional connectivity. Thus, the design matrix in the BPM is voxel-specific in contrast to the identical design matrix for all voxels in the traditional SPM analysis. Local maxima with $p < 0.05$ (FWE-corrected) were considered to be significant.

**White Matter Integrity and RSNs.** To explore the relation between WM integrity and functional connectivity, we extracted mean fractional anisotropy (FA) along the spatial course of 12 WM tracts, including those interconnecting the two cerebral hemispheres (genu, body, and splenium of corpus callosum). In addition, FA of two critical white matter tracts of the medial temporal lobe, namely the fornix and the descending cingulum, was extracted. FA is the most frequently used property of diffusion

tensor imaging (DTI) and potentially indicates local WM integrity. Full details of the procedures carried out to analyze the DTI data are described elsewhere (27).

**Large-Scale Brain System Facilitating Memory Encoding During Functional MRI Task.** To identify a network that facilitates episodic encoding, a multivariate partial-least-squares (PLS) was used to analyze fMRI data from a large population-based sample. A detailed description of the PLS analyses for the face–name paired-associate (FN-PA) fMRI task and the findings have been given elsewhere (28). In short, a data matrix was created by including each individual's fMRI block onsets and durations for each condition (i.e., encoding, retrieval, and baseline). A cross-block covariance matrix between changes in brain activity and experimental conditions was then subjected to mean centering by subtracting the mean of each column from each value of that column. Singular value decomposition was conducted on the mean-centered data matrix to reveal orthogonal latent variables (LVs), which reflect cohesive patterns of brain activity related to the experimental conditions. The first and successive LVs account for the greatest and progressively lesser amount of the cross-covariance matrix, respectively. Within each LV, voxel and design saliencies represent the relation of each voxel and experimental design to the LV, correspondingly. In addition, brain scores were computed for each LV. The brain score was obtained as a dot product of each subject's image volume and voxel saliencies of each LV to derive an estimate of how strongly each subject contributes to the pattern of each LV. Two significant LVs were identified, but only LV2 was positively correlated with performance. This LV exhibited a network encompassing the bilateral hippocampus (spatially overlapping with the hippocampal RSN) and the prefrontal cortex, which reflected greater activation during the encoding than the retrieval. The brain score of LV2, which facilitated memory performance, was considered for further investigation in relation to the hippocampal RSN.

**Hippocampal RSN and Episodic Memory Task.** To investigate whether hippocampal RSN coupling and the level of activation affect the recruitment of the hippocampus during a memory task, several analyses were carried out. In the first set of analyses, we correlated the level of activation within the left/right hippocampal regions that were strongly engaged during episodic face–name encoding [LHC: xyz = −28 −14 −16, $r$ (EM, LHC) = 0.21, $p < 0.01$; RHC: xyz = 24 −8 −18, $r$ (EM, RHC) = 0.19, $p < 0.01$; see table 2 in ref. 28] and the level of activation within the hippocampal RSN. Note that the amplitude of the HC RSN was computed as a joint metric using the TC SD and the SM maximum value, which both have the same unit of percent signal changes (for more details, see *ICA-Driven Measures of RSNs*).

In the second set of analyses, HC RSN connectivity and amplitude were related to the degree to which a larger fronto-hippocampal network, which facilitated memory performance, was recruited during episodic encoding [$r$ (brain score, EM) = 0.16, $p < 0.05$); see latent variable 2 in ref. 28]. To do this, subject-specific brain scores that reflected subjectwise level of activation within the whole network, which facilitated episodic encoding, were correlated with hippocampal RSN amplitude.

Third, we related RSN hippocampus connectivity to the level of functional connectivity of the network connected to the left hippocampus during episodic encoding (xyz = −28 −14 −16; this region strongly contributed to the network that facilitated episodic encoding during the fMRI task; see latent variable 2 and tables 2 and 3 in ref. 28). Here, a brain score represents a connectivity index across the entire network that facilitated EM performance during the fMRI task.

To further test the notion that strong HC coupling at rest restricts the degree to which the HC interacts with other brain regions during active mnemonic processing (encoding in the FN-PA task described above), older participants (55 y and older, $n$ = 284 subjects) were subdivided into two age-matched groups of high- and low-HC couplers (for each group: $n$ = 106 subjects, 66.5 ± 7.41 y of age, mean ± SD) according to a median-split analysis based on the degree of HC coupling during rest. Here, the left hippocampal cluster (LHC: xyz = −28 −14 −16; bootstrap ratio = 16.12), which reflected a high level of activation during episodic encoding (see latent variable 2 and table 2 in ref. 28), was selected as a seed region (i.e., the mean signal of all voxels within the left HC cluster was considered as the seed region). The left HC was the second most reliable cluster that contributed to the pattern expressed by LV2, which was positively correlated with episodic memory performance during the encoding task. Critically, this hippocampal cluster spatially overlaps with the hippocampal RSN. Connectivity during episodic encoding was carried out using individual parameter estimates from a left HC cluster as covariates in second-level analysis. Functional connectivity analysis yielded a network ($p <$ 0.001, FDR-corrected) that was functionally connected to LHC during episodic encoding for each group. To identify brain regions that exhibited differential connectivity to this hippocampus region as a function of hippocampal connectivity during rest (high or low couplers), a group-by-covariate interaction was performed.

**Classification of Cognitive Changes over 20 y.** Participants from a longitudinal study were classified as maintainers or average decliners based on their initial level and rate of change in episodic memory scores across 15–20 y (29, 30). The statistical classification procedures have previously been described in full detail (29) and encompassed baseline memory scores of all 1,954 participants in samples 1 (T1: 1988–1990) and 3 (T2: 1993–1995) from the Betula study and the slopes of 1,561 participants with two or more measurement points. The slopes (i.e., linear rates of cognitive change over 15–20 y) were computed for each participant through ordinary least-squares regression of the episodic memory composite on time. The slopes and baseline scores were then entered into a random effects pattern-mixture model to estimate an attrition-corrected average memory development in each of 10 age cohorts in our full sample. Each participant was classified based on how his/her initial baseline memory score and estimated rate of change compared with the average for his/her age cohort as estimated from the pattern-mixture model. To obtain an outcome measure that accounted for both initial level and slope of change in memory scores, we used the predicted final score as a cutoff measure because the predicted final score, by definition, is a linear combination of the baseline score plus rate of change multiplied by time in the study (i.e., 15 or 20 y). This allowed us to consider cognitive performance across the entire 15–20 y that the participants had been followed in our definition of successful aging. All individuals with predicted final scores greater than 1 SD from the estimated average score in each respective age cohort were classified as successful agers [denoted "maintainers" in Josefsson and colleagues (29)]. All participants falling within +1/−1 SD from the average predicted final score were classified as average decliners.

The final group size of 51 reflects the fact that 75 individuals in the imaging sample were classified as maintainers, and 24 of these were excluded based on poor image quality, health-related issues, and not reaching scanner task performance criteria set up in our previous study (30), in which exact exclusion details are provided. The average decliners were age-matched person-by-person to the maintainers, and selected into the sample based on how close they were to the average initial memory and memory change in the full sample ($n$ = 1,954/1,561). Selection of participants from the imaging sample into the average decliner group was based on the shortest standardized Euclidian distance to the average baseline cognitive test score and the average slope of cognitive

change. This metric was calculated for each age cohort in the full Betula sample (1,954 participant baseline scores and the slopes of 1,561 participants with two or more measurements). This procedure ensured that the most representative participants (i.e., those closest to the average baseline score and slope) from the imaging sample were selected into the average decliner group. Whenever a participant with the shortest Euclidian distance met any of the exclusion criteria, the person with the next shortest distance was selected instead.

We investigated the HC RSN in relation to longitudinal memory changes. We compared the functional coupling of HC RSN between 51 successful elderly persons (maintainer; age, 68.8 ± 7.1 y, mean ± SD) and 51 age-matched average decliners. In addition, we compared the functional connectivity during episodic encoding in the FN-PA task between two groups of successful and average older participants, as reported in our recent study [cf. (30)]. This was carried out using individual parameter estimates from a left HC cluster (peak xyz = −30 −14 −16) as covariates in second-level analysis. The hippocampal cluster was identified as being more engaged by the successful rather than the average participants in a group contrast of episodic memory encoding compared with baseline [cf. (30)]. To identify brain regions that exhibited differential connectivity to this hippocampus region as a function of cognitive status (successful or average decliner), a group-by-covariate interaction was performed.


1. Ashburner J (2007) A fast diffeomorphic image registration algorithm. *Neuroimage* 38(1):95–113.
2. Allen EA, et al. (2011) A baseline for the multivariate comparison of resting-state networks. *Front Syst Neurosci* 5:2.
3. Bell AJ, Sejnowski T (1995) An information-maximization approach to blind separation and blind deconvolution. *Neural Comput* 7:1129–1159.
4. Himberg J, Hyvärinen A, Esposito F (2004) Validating the independent components of neuroimaging time series via clustering and visualization. *Neuroimage* 22(3):1214–1222.
5. Erhardt EB, et al. (2011) Comparison of multi-subject ICA methods for analysis of fMRI data. *Hum Brain Mapp* 32(12):2075–2095.
6. Allen EA, Erhardt EB, Wei Y, Eichele T, Calhoun VD (2012) Capturing inter-subject variability with group independent component analysis of fMRI data: A simulation study. *Neuroimage* 59(4):4141–4159.
7. Li YO, Adali T, Calhoun VD (2007) Estimating the number of independent components for functional magnetic resonance imaging data. *Hum Brain Mapp* 28(11):1251–1266.
8. Ystad M, Eichele T, Lundervold AJ, Lundervold A (2010) Subcortical functional connectivity and verbal episodic memory in healthy elderly—A resting state fMRI study. *Neuroimage* 52(1):379–388.
9. Biswal BB, et al. (2010) Toward discovery science of human brain function. *Proc Natl Acad Sci USA* 107(10):4734–4739.
10. Damoiseaux JS, et al. (2006) Consistent resting-state networks across healthy subjects. *Proc Natl Acad Sci USA* 103(37):13848–13853.
11. Raichle ME, et al. (2001) A default mode of brain function. *Proc Natl Acad Sci USA* 98(2):676–682.
12. Smith SM, et al. (2009) Correspondence of the brain's functional architecture during activation and rest. *Proc Natl Acad Sci USA* 106(31):13040–13045.
13. Andrews-Hanna JR, et al. (2007) Disruption of large-scale brain systems in advanced aging. *Neuron* 56(5):924–935.
14. Beckmann CF, DeLuca M, Devlin JT, Smith SM (2005) Investigations into resting-state connectivity using independent component analysis. *Philos Trans R Soc Lond B Biol Sci* 360(1457):1001–1013.
15. Damoiseaux JS, et al. (2008) Reduced resting-state brain activity in the "default network" in normal aging. *Cereb Cortex* 18(8):1856–1864.
16. Glahn DC, et al. (2010) Genetic control over the resting brain. *Proc Natl Acad Sci USA* 107(3):1223–1228.
17. Jafri MJ, Pearlson GD, Stevens M, Calhoun VD (2008) A method for functional network connectivity among spatially independent resting-state components in schizophrenia. *Neuroimage* 39(4):1666–1681.
18. Liao R, McKeown MJ, Krolik JL (2006) Isolation and minimization of head motion-induced signal variations in fMRI data using independent component analysis. *Magn Reson Med* 55(6):1396–1413.
19. Power JD, Barnes KA, Snyder AZ, Schlaggar BL, Petersen SE (2012) Spurious but systematic correlations in functional connectivity MRI networks arise from subject motion. *Neuroimage* 59(3):2142–2154.
20. Van Dijk KR, Sabuncu MR, Buckner RL (2012) The influence of head motion on intrinsic functional connectivity MRI. *Neuroimage* 59(1):431–438.
21. Abou Elseoud A, et al. (2014) Altered resting-state activity in seasonal affective disorder. *Hum Brain Mapp* 35(1):161–172.
22. Yan CG, et al. (2013) A comprehensive assessment of regional variation in the impact of head micromovements on functional connectomics. *Neuroimage* 76:183–201.
23. Calhoun VD, Kiehl KA, Pearlson GD (2008) Modulation of temporally coherent brain networks estimated using ICA at rest and during cognitive tasks. *Hum Brain Mapp* 29(7):828–838.
24. Satterthwaite TD, et al. (2013) An improved framework for confound regression and filtering for control of motion artifact in the preprocessing of resting-state functional connectivity data. *Neuroimage* 64:240–256.
25. Nilsson L-G, et al. (1997) The Betula prospective cohort study: Memory, health, and aging. *Neuropsychol Dev Cogn B Aging Neuropsychol Cogn* 4(1):1–32.
26. Casanova R, et al. (2007) Biological parametric mapping: A statistical toolbox for multimodality brain image analysis. *Neuroimage* 34(1):137–143.
27. Salami A, Eriksson J, Nilsson LG, Nyberg L (2012) Age-related white matter microstructural differences partly mediate age-related decline in processing speed but not cognition. *Biochim Biophys Acta* 1822(3):408–415.
28. Salami A, Eriksson J, Nyberg L (2012) Opposing effects of aging on large-scale brain systems for memory encoding and cognitive control. *J Neurosci* 32(31):10749–10757.
29. Josefsson M, de Luna X, Pudas S, Nilsson LG, Nyberg L (2012) Genetic and lifestyle predictors of 15-year longitudinal change in episodic memory. *J Am Geriatr Soc* 60(12):2308–2312.
30. Pudas S, et al. (2013) Brain characteristics of individuals resisting age-related cognitive decline over two decades. *J Neurosci* 33(20):8668–8677.

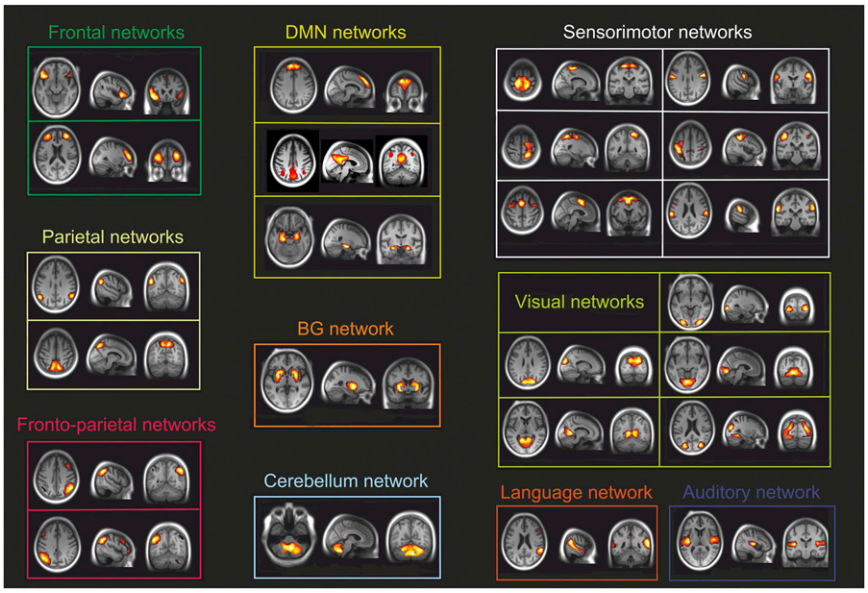


**Fig. S1.** Resting-state networks during a 6-min scan. Twenty-four out of 47 estimated components were identified (see *Methods* for details about RSN selection criteria). RSNs were divided into groups based on their anatomical and functional properties, and included basal ganglia (BG), auditory, sensorimotor, visual, cerebellar, default mode, attentional, and frontal networks. Spatial maps of each RSN are plotted as *t* statistics. Thresholding was based on the distribution of voxelwise *t* statistics to identify voxels reliably and consistently activated across subjects, using a gamma-mixture model fit controlling for FDR at 1%. The HC component included the hippocampus proper and the parahippocampal and enthorinal cortex. Posterior DMN included the posterior cingulum, cuneus, precuneus, and bilateral angular gyrus. Anterior DMN included the medial prefrontal cortex and a small portion of the posterior cingulum.

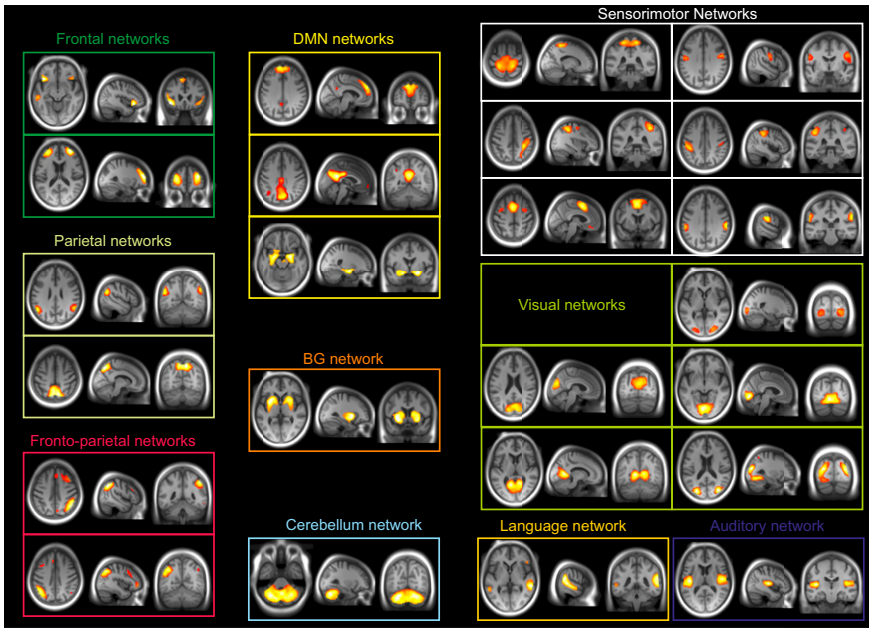


**Fig. S2.** Resting-state networks during a 6-min scan after (pre-ICA) global signal regression and (pre-ICA) motion regression (using the Friston 24-parameter model). Twenty-four out of 47 estimated components were identified (compare Fig. S1). All identified components showed strong spatial correlations ($r > 0.95$, $p < 0.0001$) with components reported in Fig. S1, where both motion parameters and global signal regression were regressed out from the ICA time courses (i.e., post-ICA). This correspondence indicated that ICA components remained strikingly similar regardless of whether motion and GSR were regressed out pre- or post-ICA.

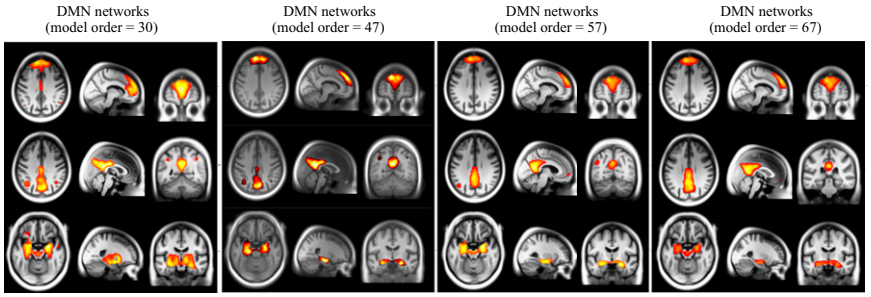


**Fig. S3.** Functional segmentation of the DMN at different functional hierarchical levels. Functional architecture of the DMN remained relatively stable at different model orders.

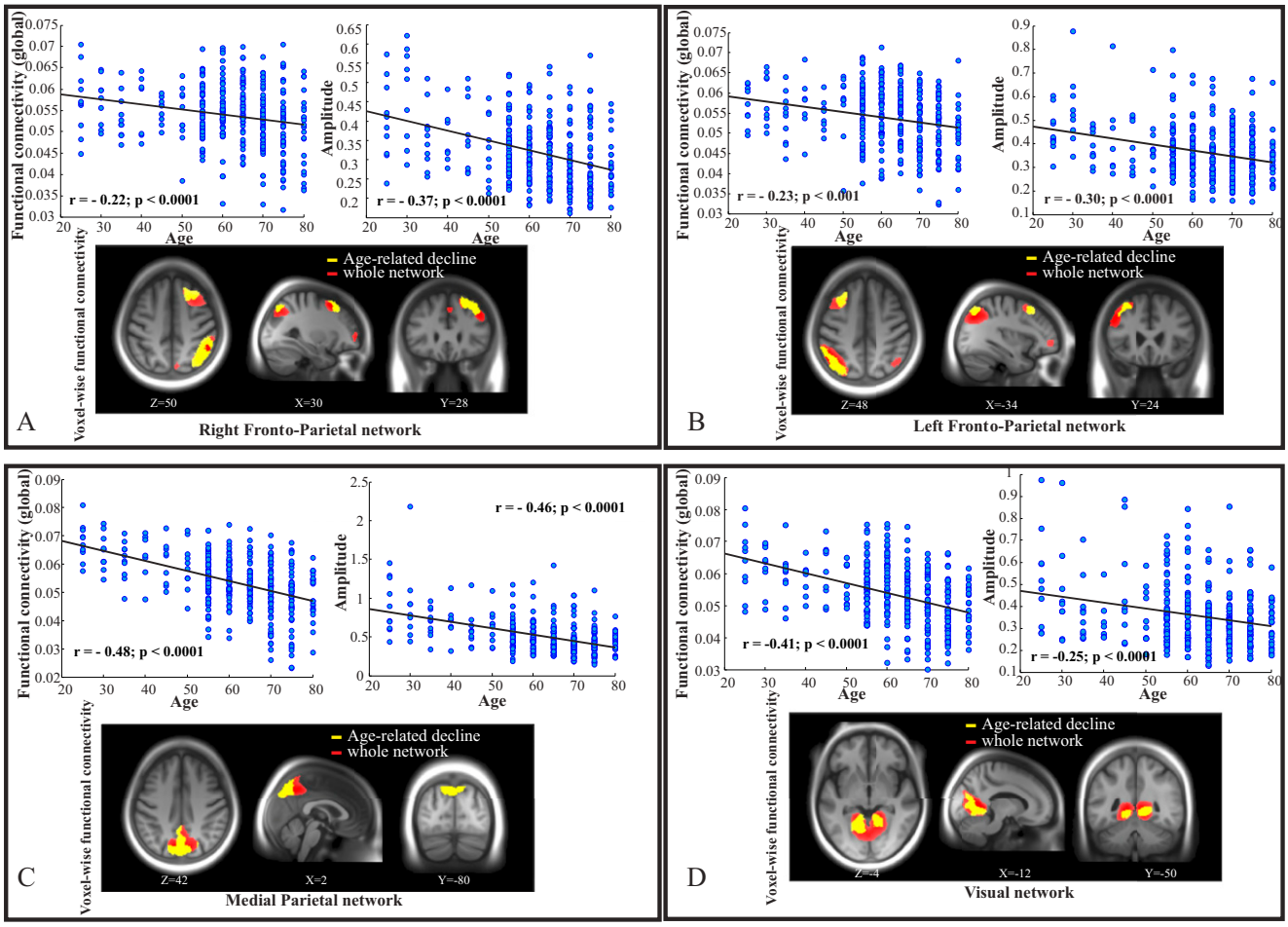


**Fig. S4.** Effect of age on three different ICA-derived measures of attentional and visual RSNs. For each RSN, the scatter plots display global functional connectivity (measured across the whole RSN network) and amplitude as a function of chronological age. The slice panels indicate brain regions (in yellow) exhibiting age-related decline within each RSN (i.e., age-related decline in voxelwise connectivity). The results of age-related decline in voxelwise connectivity are overlaid on the sample-specific template created using DARTEL. Note that regions in yellow are parts of the whole network shown in red. *A* and *B* display age-related decline in all three ICA-driven measures of the right and left fronto-parietal attentional network, respectively. *C* and *D* exhibit age-related decline in all ICA-driven measures of medial parietal and visual networks, respectively. Results for age effects were corrected for multiple comparisons [global measures: $r \geq 0.20$, $p < 0.0001$; voxelwise measures: $p < 0.05$ (FWE-corrected), $k > 20$]. No age-related increases were observed for these RSNs.

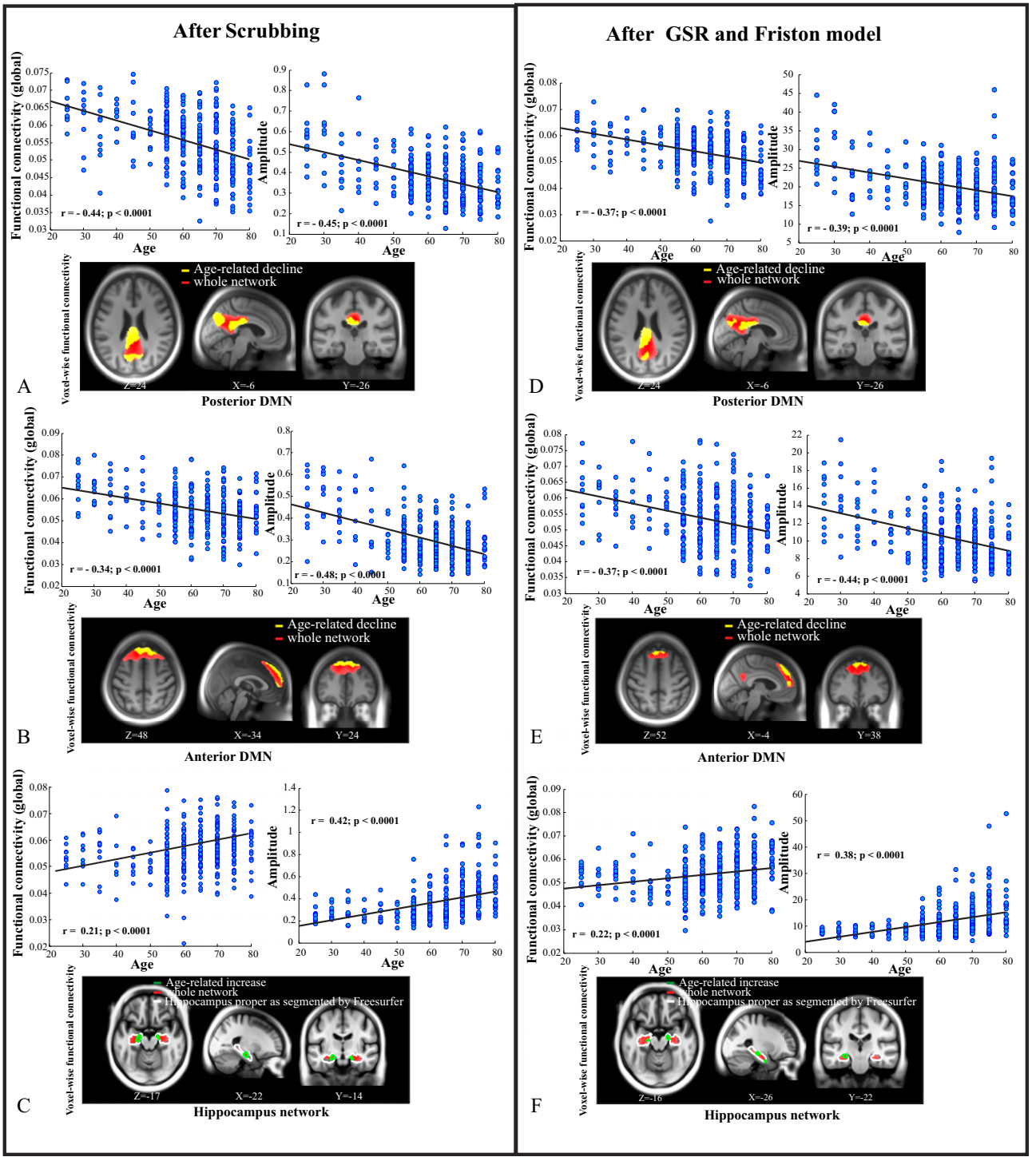


**Fig. S5.** Effect of age on ICA-driven measures of the HC and DMN after two different motion correction methods. Age-related alteration of the posterior (*A* and *D*) and anterior (*B* and *E*) DMN and the HC RSN (*C* and *F*) for three different ICA-driven measures (voxelwise connectivity, global connectivity, and amplitude) after pre-ICA motion correction (scrubbing and the Friston model) and global signal regression. Additionally, we controlled for framewise displacement in all reported correlations (see Fig. 1 for more details).

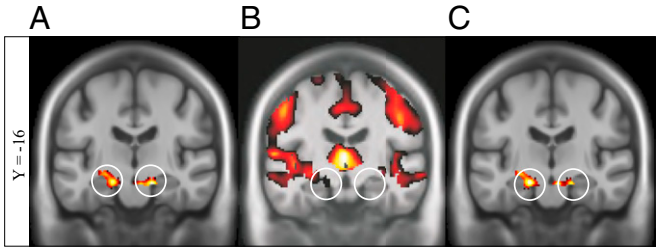


**Fig. S6.** Increased hippocampal RSN in relation to gray matter volume. Results of the multimodal BPM analysis overlaid on the sample-specific template created using DARTEL. Circles indicate structural and functional alterations in the bilateral HC. (*A*) Regression analysis reflecting age-related increases in functional connectivity (left HC: xyz = −18 −14 −18, $t_{334}$ = 9.33; right HC: xyz = 16 −10 −14, $t_{334}$ = 5.63). (*B*) Regression analysis demonstrating age-related gray matter volume loss. (*C*) Regression analysis indicating age-related differences in HC coupling after controlling for local GM loss (left HC: xyz = −18 −14 −18, $t_{334}$ = 9.29; right HC: xyz = 16 −10 −14, $t_{334}$ = 5.60); age-related elevation of HC connectivity persisted after controlling for GM volume). Results were thresholded at $p < 0.05$ (FWE-corrected; $k > 20$).

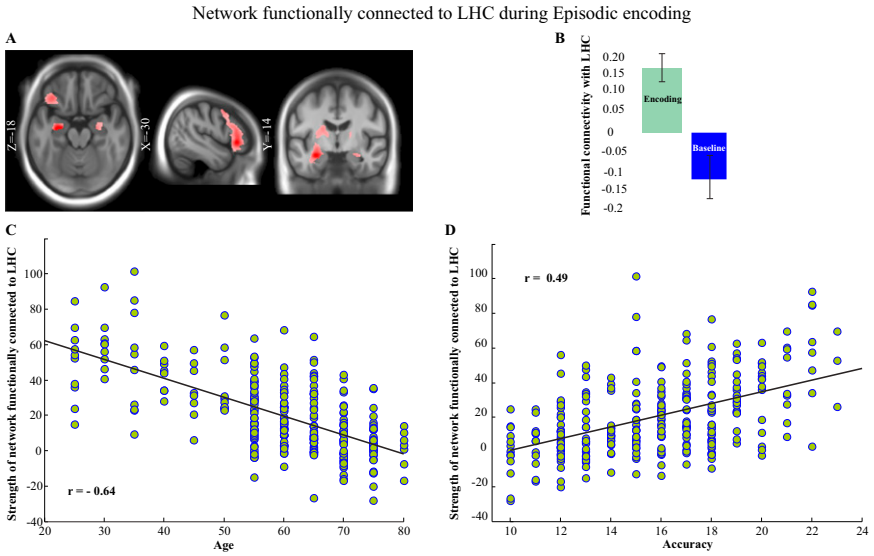


**Fig. S7.** Network functionally connected to LHC during episodic encoding. Singular images for behavioral and seed latent variable for the left HC (xyz = −28 −14 −16), which reflected a high level of activation during episodic encoding (see latent variable 2 and table 2 in ref. 28). Note that the left HC was the second most reliable cluster (bootstrap ratio 16.12) that contributed to the pattern expressed in LV2. (*A*) Singular images for a significant LV ($p < 0.001$), which exhibited greater functional connectivity with LHC during episodic encoding relative to baseline. Regions with bootstrap ratio >4 (corresponding approximately to $p < 10^{-4}$) are shown in red. These regions were functionally connected to LHC during episodic encoding. (*B*) Seed LV during episodic encoding and baseline. Error bars denote 95% confidence intervals defined by SEs of the bootstrap estimate. Nonoverlapping error bars suggest that the level of functional connectivity to LHC was greater during encoding than baseline. (*C* and *D*) Strength of the functional connectivity as a function of age and accuracy.

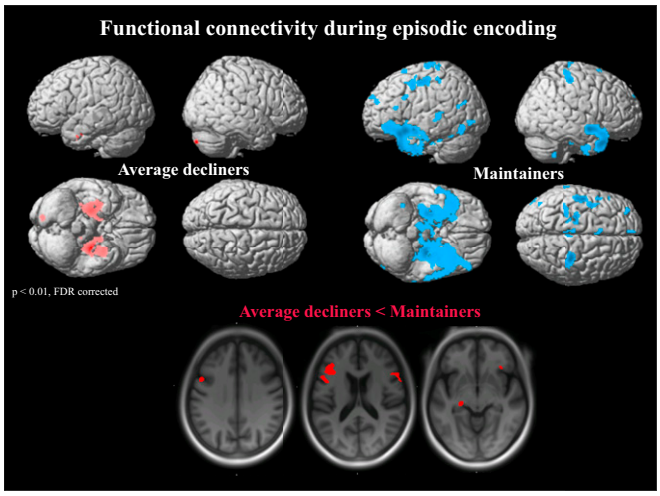


**Fig. S8.** Hippocampal RSN in relation to task-induced recruitment in individuals with maintained or declining episodic memory over time. Render figures show brain regions functionally connected to LHC (xyz = −30 −14 −16) during episodic encoding in decliners (red) and maintainers (blue). The hippocampal cluster was identified as being more engaged by the successful rather than the average participants in a group contrast of episodic memory encoding compared with baseline. Decliners who exhibited high HC coupling during rest engaged a less extensive memory network compared with maintainers who showed lower HC coupling during rest. The slice panels show brain regions that exhibited greater functional connectivity to LHC during encoding in maintainers compared with decliners (left inferior frontal gyrus: xyz = −40 22 14, $t_{48}$ = 4.05; right inferior frontal gyrus: xyz = 60 18 18, $t_{48}$ = 3.93; left HC: xyz = −24 −26 −8, $t_{48}$ = 3.88).

**Table S1. Correlation of ICA measures of DMN hubs with neuropsychological measures and integrity of selected white matter pathways**

| Network | EM | BD | Genu | Body | Splenium | Fornix |
|---|---|---|---|---|---|---|
| Not corrected for age | | | | | | |
| Posterior DMN (con) | 0.22* | 0.33** | 0.15* | 0.22** | 0.18** | 0.34** |
| Posterior DMN (amp) | 0.12* | 0.20** | NS | NS | 0.11* | 0.18** |
| Anterior DMN (con) | 0.10* | NS | | | | |
| Anterior DMN (amp) | 0.15** | NS | | | | |
| HC network (con) | −0.25** | −0.15* | −0.14* | −0.12* | NS | −0.31** |
| HC network (amp) | −0.27** | −0.23** | −0.27** | −0.27** | −0.15* | −0.40** |
| Corrected for age | | | | | | |
| Posterior DMN (con) | NS | 0.16** | NS | NS | NS | 0.12* |
| Posterior DMN (amp) | NS | NS | NS | NS | NS | NS |
| Anterior DMN (con) | NS | NS | | | | |
| Anterior DMN (amp) | NS | NS | | | | |
| HC network (con) | −0.17** | NS | NS | NS | NS | −0.22** |
| HC network (amp) | −0.17** | NS | −0.11* | −0.13* | NS | −0.22** |

*$p < 0.05$; **$p < 0.005$. amp, amplitude of a network; BD, block design; body, body of corpus callosum; con, global functional connectivity within a network; EM, episodic memory; genu, genu of corpus callosum; NS, not significant; splenium, splenium of corpus callosum. We controlled for sex and a motion parameter (framewise displacement) in all analyses.